Journal of Cluster Science (2018) 29:251–266
https://doi.org/10.1007/s10876-017-1324-8

ORIGINAL PAPER

Solution, Solid-State Two Step Synthesis and Optical Properties of ZnO and SnO_2 Nanoparticles and Their Nanocomposites with SiO_2

C. Diaz[1] · M. L. Valenzuela[2] · M. Segovia[1] · K. Correa[1] · R. de la Campa[3] · A. Presa Soto[3]

Received: 6 October 2017 / Published online: 27 December 2017

Abstract

Nanostructure luminescent ZnO and SnO_2 materials are prepared by a two-step solid-state method based on the solution preparation of the macromolecular precursors $ZnCl_2$·Chitosan and $SnCl_2$·Chitosan having different ratios (1:1, 1:5 and 1:10), their pyrolysis under air at 800 °C. The pyrolytic ZnO and SnO_2 nanomaterials show a dependence of the particle size, morphology and luminescent properties with the ratio [metal/polymer] in the MCl_2·Chitosan precursors. Thus, ZnO semiconductor materials exhibit luminescence spectra with several emission at 440 nm corresponds to a radiative transition of an electron from the shallow donor level of oxygen vacancies, and the zinc interstitial, to the valence band. On the other hand, the photoluminescence spectrum of the nanostructured SnO_2 shows an intense blue luminescence at a wavelength of 420 nm which may be attributed to oxygen-related defects that have been introduced during the growth process of the nanoparticles. Additionally, whereas SnO_2 was successfully incorporated into SiO_2 structure (SnO_2//SiO_2) by pyrolysis of solid-state mixtures of the precursors $SnCl_2$·Chitosan in the presence of SiO_2, the same reaction carried out with $ZnCl_2$·Chitosan precursors led to a mixture of Zn_2SiO_4 and SiO_2. Thus, this new methodology yields nanostructured semiconductor materials, ZnO and SnO_2, suitable for optoelectronic and sensor solid-state devices.

Keywords Solid-state synthesis · Chitosan · SnO_2·SiO_2 · ZnO·SiO_2

Introduction

Metal oxides materials are, in general, very useful semiconductors with a wide band gap spanning the visible and UV, an interesting electronic properties [1, 2], and notable catalytic application [3, 4]. Among the most important semiconductor metal oxides, SnO_2 [5] and ZnO [6] have been extensively studied due to their interesting and practical applications [7]. Thus, SnO_2 is a wide band gap n-type semiconductor with significant importance in several technological applications such as gas sensing, Li-ion batteries, and solar cells [8, 9]. For instance, it has been widely used as sensor in H_2 and CO detection [7]. Although several synthetic methods in solution have been reported for the preparation of SnO_2 materials [8, 9], only few solid-state methods leading to well characterize nanostructured SnO_2 materials have been described to date [10]. On the other hand, nanostructured ZnO is one of the most promising nanomaterials to be used in sensors due principally to its biocompatibility, chemical and photochemical stability, high specific surface area, optical transparency, electrochemical activity, and high electron mobility [6]. For instance, nanostructured ZnO materials have been successfully employed in the detection of biological molecules [11]. As above (i.e. nanostructured SnO_2 materials), only few solid-state methods have been reported to date for the preparation of well-defined ZnO materials [11, 12].

Electronic supplementary material The online version of this article (https://doi.org/10.1007/s10876-017-1324-8) contains supplementary material, which is available to authorized users.

✉ M. L. Valenzuela
maria.valenzuela@uautonoma.cl

[1] Departamento de Química, Facultad de Ciencias, Universidad de Chile, Las Palmeras 3425, Casilla 653, Ñuñoa, Santiago, Chile

[2] Instituto de Ciencias Químicas Aplicadas, Inorganic Chemistry and Molecular Materials Center, Facultad de Ingeniería, Universidad Autónoma de Chile, el Llano Subercaseaux, 2801 San Miguel, Santiago, Chile

[3] Departamento de Química Orgánica e Inorgánica (IUQOEM), Facultad de Química, Universidad de Oviedo, Julián Clavería s/n, 33006 Oviedo, Spain

Generally, the incorporation of metal-oxide nanoparticles into solid sensors is problematic when those have been produced via a solution phase method, because the solid-state isolation of the nanoparticles usually causes the nanoparticle agglomeration [13]. In this regard, the synthesis of nanoparticles directly from a solid-state approach might represent a more reliable method to achieve the incorporation of metal-oxides into sensors. Consequently the development of new solid-state methods to prepare metal-oxide nanoparticles is sought after. We have previously reported two solid-state methods allowing the synthesis of different metallic nanostructured materials (M, M_xO_y, and $M_xP_yO_z$) for a range of transition, valve and noble metals. The first methodology employed organometallic derivatives directly linked to poly- and cyclotriphosphazenes as molecular precursors of the metallic nanostructure [14–17], while the second used solid-state mixtures of an appropriate organometallic moiety and cyclotriphosphazenes not possesing any coordinative functional group (i.e. cyclospirophosphazenes of general formula $[N = P(O_2C_{12}H_8)]_3$) [18]. Both yielded the metal oxides together with pyrophosphate phases of the corresponding metal. For instance, when metals and metalloids were used both phases were observed, i.e. the metal oxide and the pyrophosphate. However, with noble metals, for which the formation of oxides or pyrophosphates is thermodynamically unfavored, the reduction with CO produced nanostructured M° materials during the molecular decomposition by pyrolysis [18].

Among the different solid-state polymer templates that can be used for the synthesis of nanostructured metal oxides, Chitosan is one of the most promising macromolecules. Chitosan is derived from chitin, which is the second most abundant natural polymer after cellulose, and can be extracted mainly from shrimp and krillby deacetylation with strong alkali bases [19–21]. The structure of Chitosan has been elucidated from molecular and crystal structure determination of both the hydrated and non-hydrated forms [22]. Chitosan is a biodegradable, biocompatible and non-toxic polysaccharide that, owing their interesting properties, it has received considerable attention in environmental, agricultural and biomedical applications [23–25]. One of the most interesting properties of Chitosan is related to its inherential high capacity to establish metal macromolecular complexes, and their high efficiency for metal uptaking from aqueous solutions [26–28]. To date, two metal complexation models are proposed; the bridge model (I) [29] in which chitosan metal complexes are created when both, amino (two or more) and hydroxyl side groups of the main chain are binded to the same metal center (intra- or inter-molecular complexation may occur between the metal-ion and amine and hydroxyl groups from the same or different chains); and the pendant model (II), in which only one amine or hydroxyl group is acting as a pendant ligand. Studies based on ESR [30] and IR [31] suggested that the bridge model (I) is the most likely coordination pathway, whereas other studies based on X-ray [29] suggested the pendant model (II) as the most likely coordination mode. In consequence, the structure of macromolecular metal complexes of Chitosan is, so far, not well known [30].

Here, we report a straightforward solution solid-state novel two-step methodology to prepare stoichiometric and crystalline SnO_2 and ZnO metal-oxides nanoparticles. The method consists of the pyrolysis under air at 800 °C of the macromolecular complexes $ZnCl_2$·Chitosan and $SnCl_2$·-Chitosan, in which the chitosan is acting as solid state template, for the growth of the metal oxide nanoparticles. We studied the influence of the polymer/metal molar ratios over the final properties of the nanostructured metal-oxides (SnO_2 and ZnO), demonstrating that chitosan is acting as a valuable solid template that allows the formation of SnO_2 and ZnO nanoparticles with control of the particle size, morphology, and luminescent properties. Also, here we present a method to incorporate SnO_2 and ZnO metal-oxides into SiO_2 structure by pyrolysis of the MCl_2·Chitosan (M=Zn and Sn) precursors in the presence of SiO_2 generated by a sol–gel method. The Uv–vis and photoluminescence properties of the synthesized metal-oxides were also studied.

Experimental

$ZnCl_2·2H_2O$ and $SnCl_2·6H_2O$ from Aldrich were used as received. Chitosan (Aldrich) of low molecular weight was also used as received. An estimation of the molecular weight was obtained by viscosity measurements and the Mark–Houwink equation. Thus, using parameters [h] previously reported by Brugnenotto et al. [31], an aqueous solution of acetic acid, NaCl, and urea as a solvent, a value of $M_W = 61{,}000$ was estimated. All the reactions were performed using CH_2Cl_2 as solvent.

Synthesis of the Polymeric Precursors $ZnCl_2$·Chitosan and $SnCl_2$·Chitosan

A typical procedure is described as follows: In a Schlenk flask, an appropriate amount of metallic chloride ($ZnCl_2·2H_2O$ or $SnCl_2·6H_2O$) and Chitosan were suspended in CH_2Cl_2 at different [Chitosan/MCl_2] molar ratios (1:1; 1:5, and 1:10). The heterogeneous mixture was stirred at room temperature for a given time (reaction time and additional details for each metal chloride reaction are given in Table S1 of Supplementary Data). After removing the supernatant solution by decantation, the remained solid

was dried under reduced pressure to give white materials. Due to their insolubility, the characterization of the precursors was performed by ^{13}C-CP-MAS NMR spectroscopy, elemental analysis, FT-IR spectroscopy, and TG/DSC analysis see Table S2 of Supplementary Data. Approximate metal content was estimated from the elemental analysis and the TGA curves.

Incorporation of SnO_2 and ZnO into SiO_2

SiO_2 was prepared according with the literature procedures. Briefly, tetraethoxysilane (TEOS), ethanol, and acetic acid in a molar ratio of 1:4:4, were mixed with water (nanopure), and the mixture were stirring for 3 day. The obtained gel was dried at 100 °C under reduced pressure in

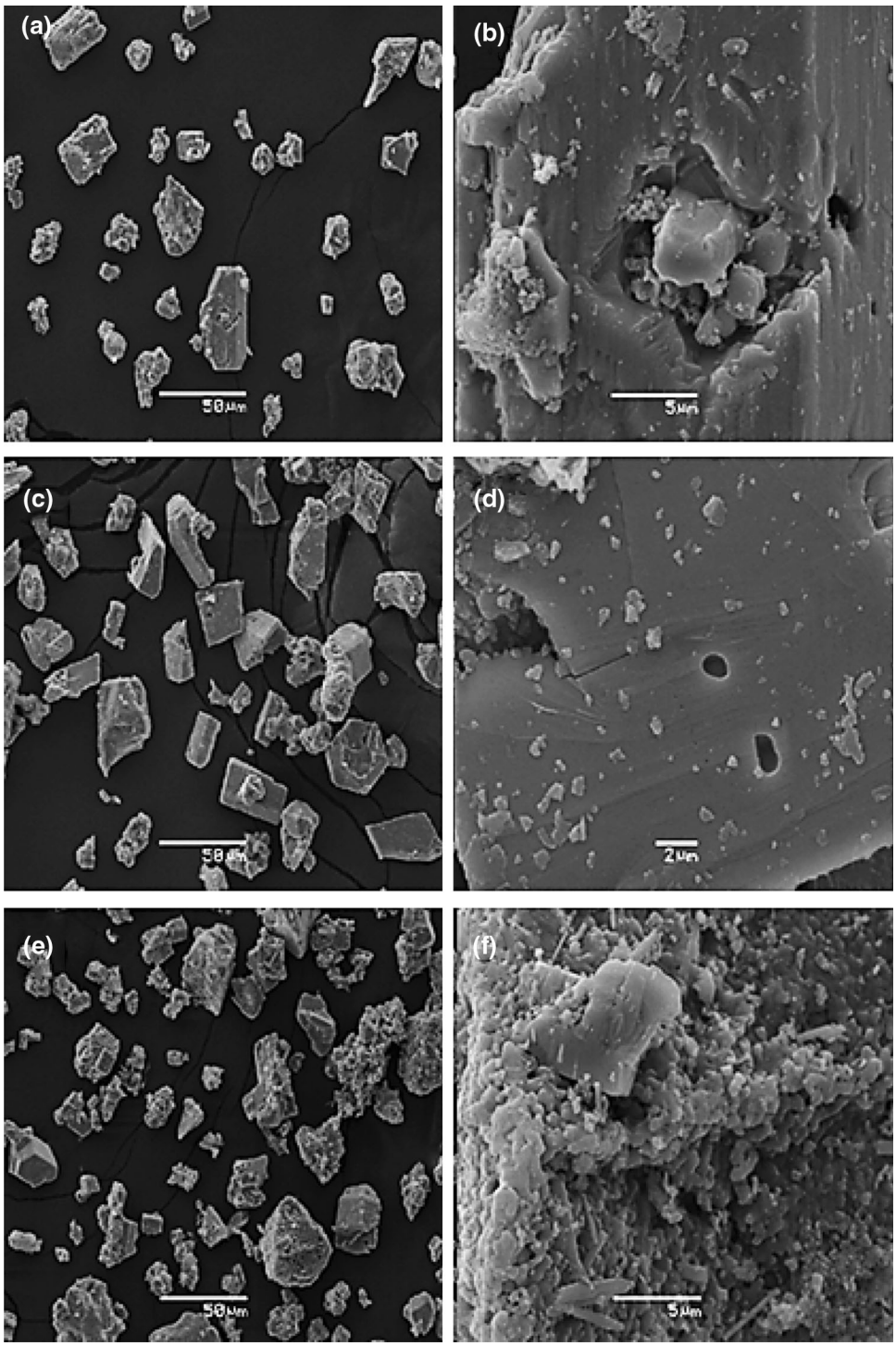

Fig. 1 SEM images at different magnifications of ZnO nanomaterials synthesized from $ZnCl_2$·Chitosan precursors having different [polymer/metal] molar ratios: **a**, **b** 1:1, **c**, **d** 1:5 and **e**, **f** 1:10

a vacuum furnace. Mixtures of solid precursors [$ZnCl_2$·Chitosan] and [$SnCl_2$·Chitosan] were calcined at 800 °C for 2 h under air in the presence of as prepared SiO_2.

Pyrolysis of the Precursors

Pyrolysis experiments were performed using 0.05–0.15 g of the metallic precursors, $ZnCl_2$·Chitosan and $SnCl_2$·Chitosan, in alumina boats. The samples were heated in a furnace (Daihan oven model Wise Therm FHP-12) under a

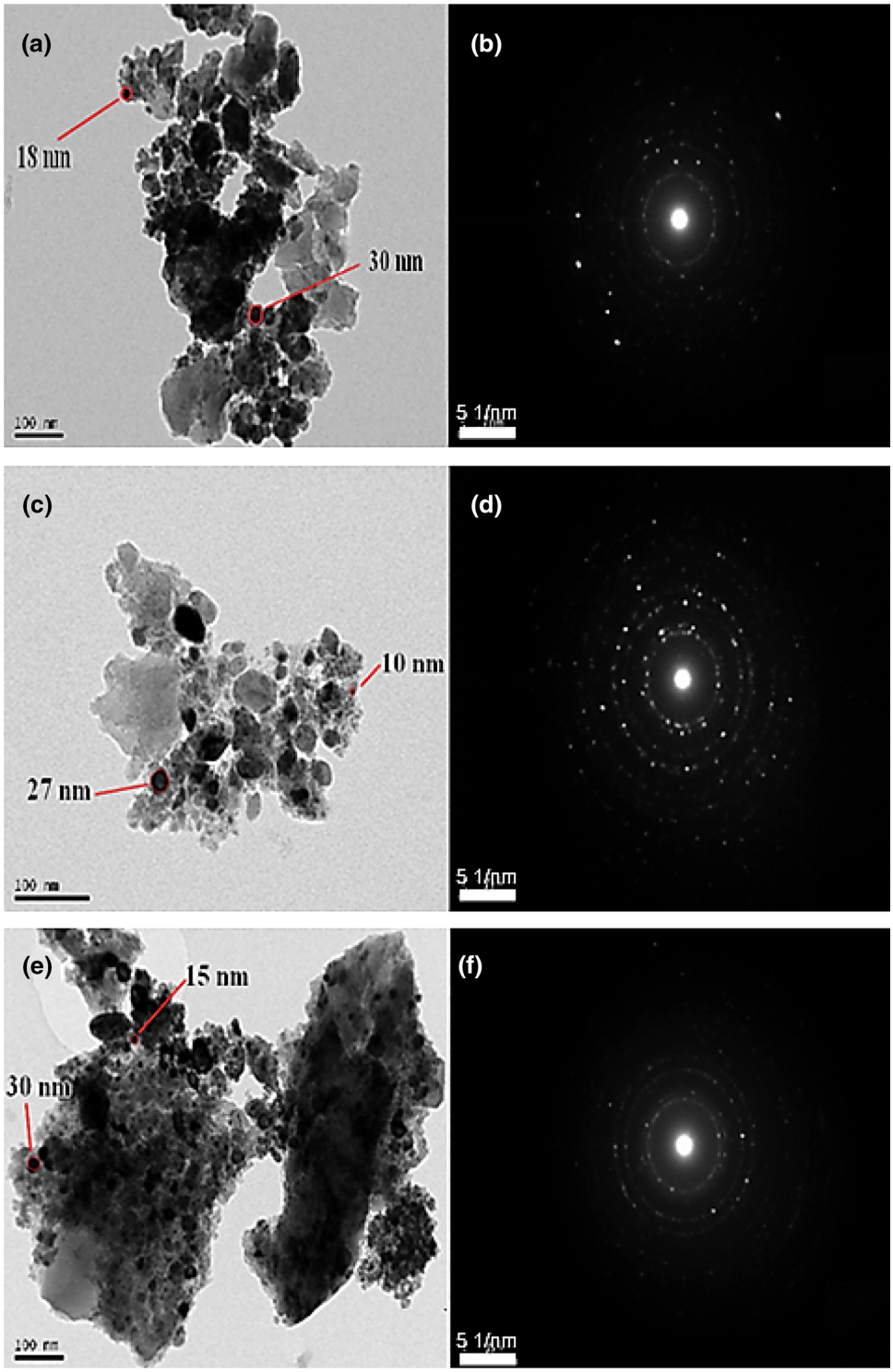

Fig. 2 TEM images (left) and electron diffraction patterns (right) of the ZnO prepared from $ZnCl_2$·Chitosan in [polymer/metal] molar ratios of 1:1 (**a**, **b**), 1:5 (**c**, **d**), and 1:10 (**e**, **f**)

flow of air from 25 °C to upper temperature limits of 200 °C, and then to 800 °C, followed by annealing at 800 °C for 2–4 h. The heating rate was fixed at 10 °C min^{-1} for all experiments.

Characterization of the Pyrolytic Products

The solid pyrolytic samples were characterized by X-Ray powders diffraction (XRD), scanning electron microscopy (SEM), high resolution transmission electron microscopy (HR-TEM), Fourier transform infra-red (FT-IR) spectroscopy, and thermogravimetric (TGA) and differential scanning calorimetric (DSC) analysis. SEM images were acquired with a Philips EM 300 scanning electron microscope. Energy dispersive X-ray analysis (EDAX) was performed on a NORAN Instrument micro-probe attached to a JEOL 5410 scanning electron microscope. TEM data were acquired using a JEOL SX100 and a JEOL 2011 transmission electron microscope. HRTEM observations were performed using a JEOL 2000FX microscope at 200 kV. TEM samples were prepared by dispersing the pyrolyzed material onto copper grids and dried at room temperature. For high-resolution examination of graphitic carbons, flakes of sonicated carbons were dispersed on grids and examined under the SEM to determine their thickness. X-ray diffraction (XRD) was conducted at room temperature on a Siemens D-5000 diffractometer with θ–2θ geometry. XRD data was collected using Cu-*Kα* radiation (40 kV, 30 mA). FTIR measurements were performed on a Perkin Elmer FT-IR spectrophotometer model Spectrum BXII.

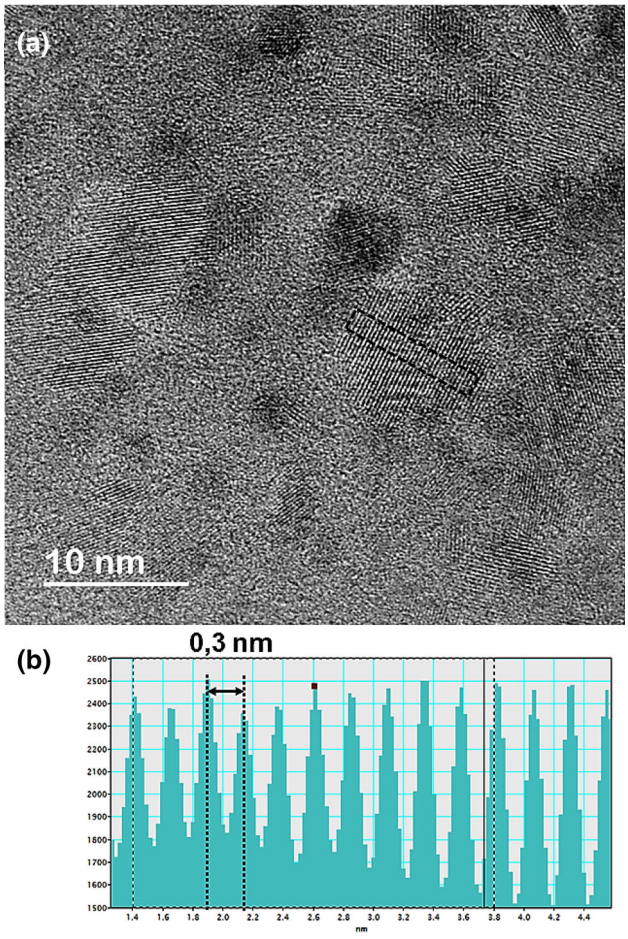

Fig. 3 **a** HR-TEM of ZnO prepared from the 1:1 $ZnCl_2$·Chitosan precursor. **b** Measured lattice spacing of adjacent lattice planes of ZnO materials (dashed black squared area in **a**

Results and Discussion

The direct reaction of the metallic dichlorides, $SnCl_2$ and $ZnCl_2$, with Chitosan in CH_2Cl_2, yielded air stable polymeric precursor of general formula $ZnCl_2$·Chitosan and $SnCl_2$·Chitosan as a white solids. The reaction between the partially soluble Chitosan and the insoluble metallic chlorides, MCl_2 (M=Zn or Sn) ocurred in heterogeneous phase. The equilibrium of the reaction was slowly moved toward the formation of very insoluble $ZnCl_2$·Chitosan and $SnCl_2$·Chitosan precursors respectively. Due to the low solubility of the MCl_2 chlorides in CH_2Cl_2, the synthesis of the precursors was very slow, taking about 2 weeks to conclusion. The metal content in the precursors was determined by both elemental and TGA analysis. By both techniques the values were varying consistently from 89 to 94% of the initial amount of MCl_2 used in each reaction (see Table S2 in Supplementary Materials). This result demonstrated that almost all the metal chloride used in the reaction is coordinated to chitosan. This is of pivotal importance in order to control the polymer/metal ratio in the final $ZnCl_2$·Chitosan and $SnCl_2$·Chitosan precursors. Both polymeric precursors were analyzed by ^{13}C-CP-MAS NMR spectroscopy showing the presence of Chitosan in the macromolecular complexes (see S3 of Supplementary Data) [31–33]. Moreover, the peaks were slightly shifted (downfield) with respect to those of free Chitosan evidencing the coordination of the metallic moiety to the polymeric backbone. The down field shifting of the signals was more pronounced in the carbon directly linked to the coordinating NH_2 group (C_1 of the precursors was shifted (ca. 1 ppm) from that of chitosan (see S3 of Supplementary Materials). However, this effect was not observed in the 1:10 $ZnCl_2$·Chitosan precursor because the metal content was very low (see S3 of Supplementary Materials). These deshelling in the ^{13}C-CP-MAS NMR signals was also observed in similar [Pt]·Chitosan complexes [32].

TGA/DTA analyses also provided evidences of the coordination of Zn and Sn metal centers to the polymer backbone. For instance, the thermogram of the

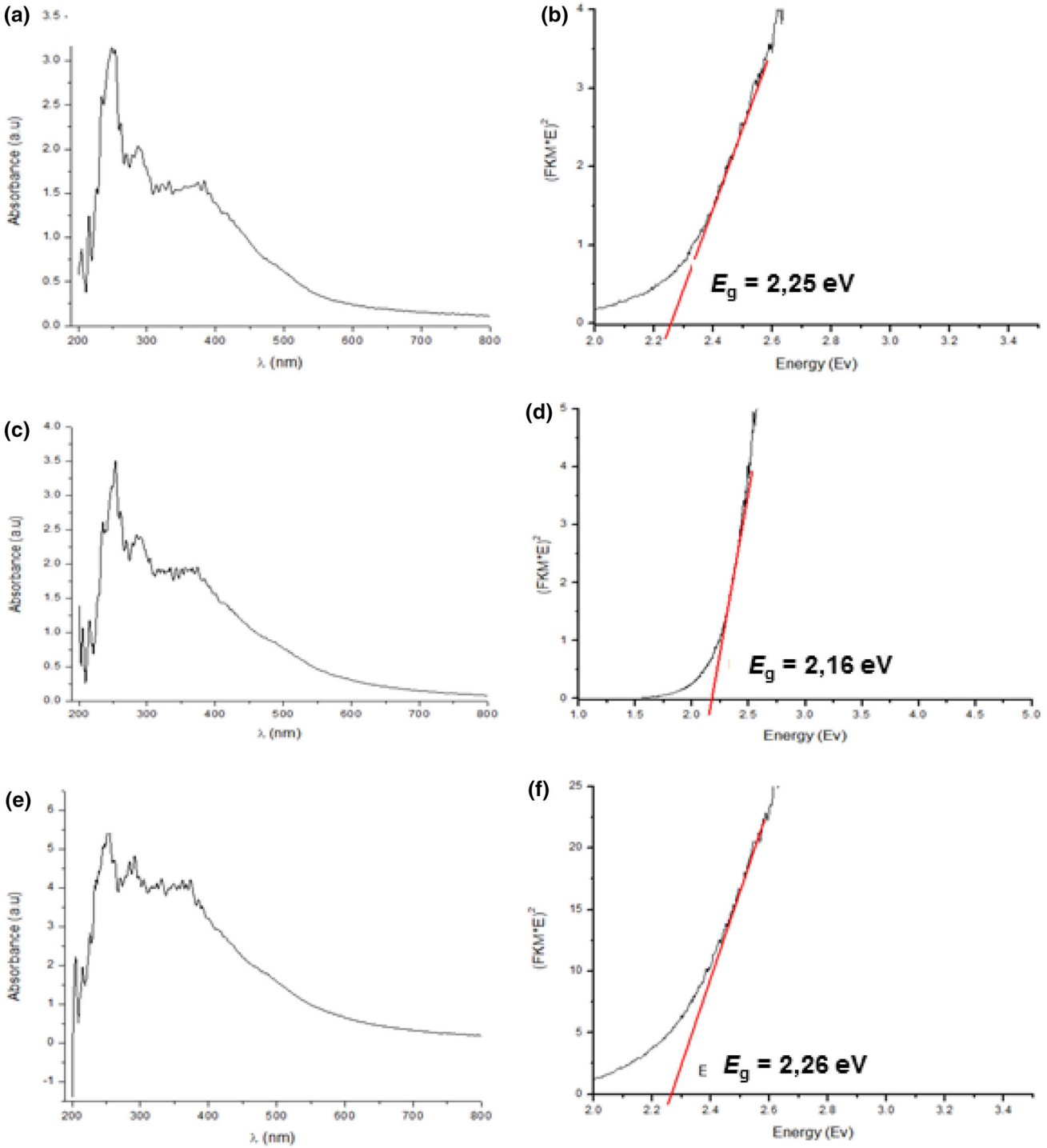

Fig. 4 Uv-vis absorption and reflectance data (converted to Kubelka–Munk spectra) of ZnO nanoparticles created by the $ZnCl_2$·Chitosan precursors at different [polymer/metal] molar ratios: **a** 1:1, **c** 1:5, and **e** 1:10. Tauc's plot, $(\alpha h\nu)^2 = A(h\nu - E_g)$ having the optical band energy (E_g) of ZnO nanoparticles created by the $ZnCl_2$·Chitosan precursors at different [polymer/metal] molar ratios: **b** 1:1, **d** 1:5, and **f** 1:10

$ZnCl_2$·Chitosan precursor in 1:1 molar ratios exhibited very different weight loss pattern with respect to that of the free Chitosan (see S4 Supplementary Data) [34]. Indeed, whereas the DTA curve of the free Chitosan showed a strong sharp exothermic peak at 290 °C, and two more exothermic peaks at 550 and 650 °C, the DTA curve of the Chitosan·$ZnCl_2$ (1:1) precursor showed a peak at 250 °C, and only one broad peak at 550 °C due to the formation of

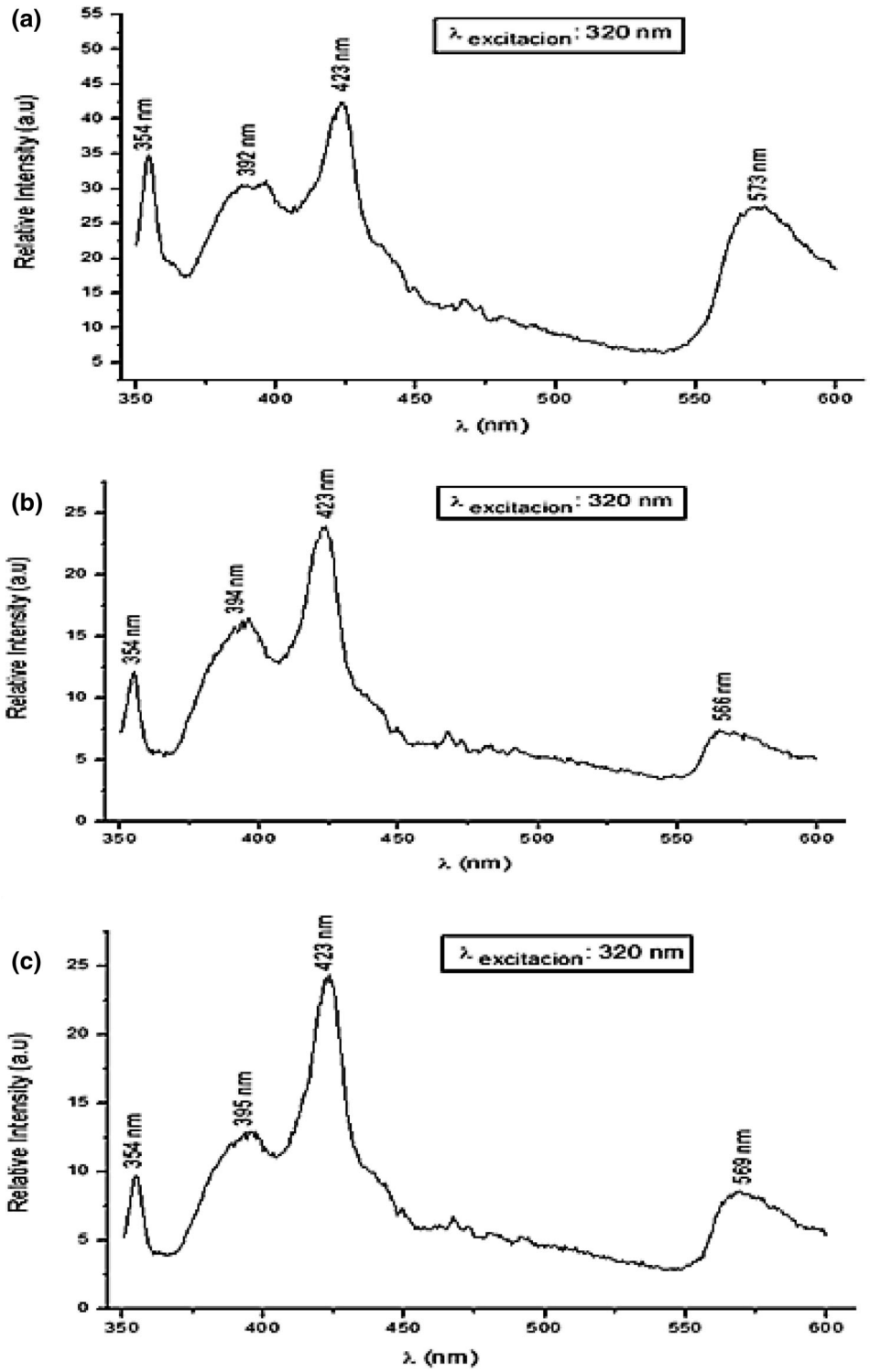

Fig. 5 Luminescence spectra of ZnO nanoparticles created by the $ZnCl_2$·Chitosan precursors at different [polymer/metal] molar ratios: **a** 1:1, **b** 1:5, and **c** 1:10

ZnO, which evidenced the coordination of the Zn^{2+} centers to the chitosan. Also the final ceramic residue at 800 °C of the Chitosan·$ZnCl_2$ (1:1), precursor was higher (90% of its initial mass) than that of chitosan as a result of the metal moiety coordination (non-coordinate MCl_2 species were eliminated during the CH_2Cl_2 filtration). Similar behavior was observed for the $ZnCl_2$·Chitosan having different metal loadings (1:5 and 1:10), as well as for the $SnCl_2$·Chitosan precursors (1:1, 1:5 and 1:10).

X-ray powder diffraction (XRD) patters of the pyrolytic products from $ZnCl_2$·Chitosan precursors (1:1. 1:5, and 1:10) showed the main peaks corresponding to hexagonal

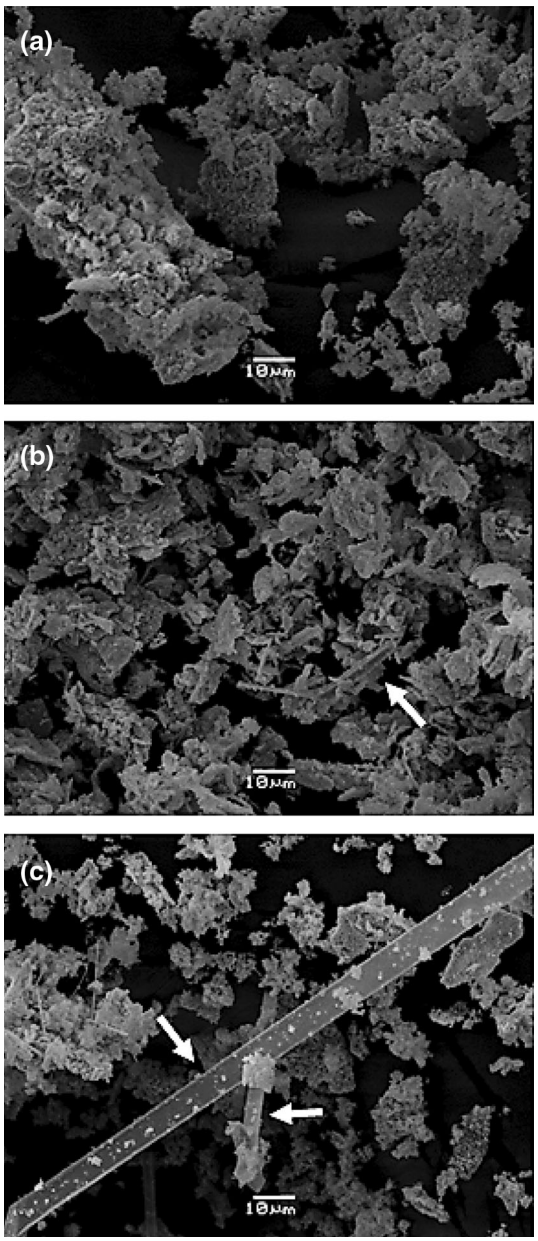

Fig. 6 SEM images, showing the morphology of the SnO_2 materials prepared from precursor $SnCl_2$·Chitosan in [polymer/metal] molar ratios of 1:1 (**a**), 1:5 (**b**), and 1:10 (**c**). White arrows highlight the nanorod-like morphologies

phase of the ZnO. For instance, the pyrolysis of 1:1 $ZnCl_2$·Chitosan precursors led to a diffractogram pattern with peaks at 2θ values of 31.88°, 34.53°, 36.36° and 56.70°, corresponding to the (100), (002), (101) and (110) planes of the hexagonal phase of the ZnO (see Figure S5 in the Supplementary Data). The analysis of these hexagonal ZnO phases by SEM clearly showed a dependence of the morphology with the [polymer/metal] molar ratio of the precursors (Fig. 1). Thus, when $ZnCl_2$·Chitosan having [polymer/metal] molar ratios of 1:1 and 1:5 were used as precursors, SEM images showed very compacted and homogeneous ZnO morphologies (see Fig. 1a, b respectively), whereas when the 1:10 [polymer/metal] molar ratio precursor was used, porous ZnO materials were obtained (see Fig. 1c). The higher dispersion of the metal moiety in the 1:10 $ZnCl_2$·Chitosan precursor with respect to that of the 1:1 and 1:5, may explain the less homogeneous texture of the 1:10 precursor, leading to porous ZnO materials.

The EDX analysis of the materials prepared from the different $ZnCl_2$·Chitosan precursors ([polymer/metal] molar ratios of 1:1, 1:5, and 1:10), confirmed the presence of ZnO materials by the presence of Zn and O elements (see Figure S6 in the Supplementary Data).

The as obtained ZnO materials were also analyzed by TEM. As it is usually found from a variety of preparation methods involving thermal treatments, a wide particle size distribution was observed (see Fig. 2). However, a closely look to the micrographs showed a slightly different size distribution of the nanostructures of ZnO depending of the different [polymer/metal] molar ratios used in the $ZnCl_2$·Chitosan precursors (see Fig. 2). Thus, the smallest size ZnO nanoaggregates were observed when a 1:5 [polymer/metal] molar ratio of the $ZnCl_2$·Chitosan precursor was used (see Fig. 2c). Interestingly, at this [polymer/metal] molar ratio of the $ZnCl_2$·Chitosan precursor (1:5), we observed the highest crystallinity in the electron diffraction pattern of the ZnO nanoparticles. So, at 1:5 [polymer/metal] molar ratio the crystallization of the hexagonal phase of the ZnO nanoparticles is favored with respect to the 1:1 and 1:10 [polymer/metal] molar ratios.

HR-TEM analysis was performed using a single crystal ZnO nanoparticles obtained from the 1:1 $ZnCl_2$·Chitosan precursor (see Fig. 3). The single ZnO nanoparticle exhibited a particle size ranging from 6 to 40 nm. The measured lattice spacing of adjacent lattice planes was about 0.30 nm, corresponding to the (100) plane of hexagonal ZnO nanoparticles and grew along the [100] direction (see Fig. 3b).

ZnO is an n-type semiconductor with a wide band gap of 3.37 eV in bulk. We studied the diffuse reflectance spectra (DRS) of the ZnO materials prepared from the 1:1. 1:5, and 1:10 $ZnCl_2$·Chitosan precursors at room temperature (see Fig. 4a, c and e. The reflectance data was converted to Kubelka–Munk equation using standard procedures). ZnO samples showed a strong absorption band in the region between 200 and 400 nm. Thus, the absorptions of ZnO are mainly located at the UV region, not observing intense absorptions in the visible region. This result is attributed to the direct band gap of ZnO due to electron transitions from the valence to the conduction band (O_{2p}–Zn_{3d}) [35]. The optical band-gap energies of the ZnO materials were estimated from Tauc'splot, $(\alpha h\nu)^2 = A(h\nu - E_g)$ (see Fig. 4b, d and f). The band gap values of the E_g were found to be 2.25

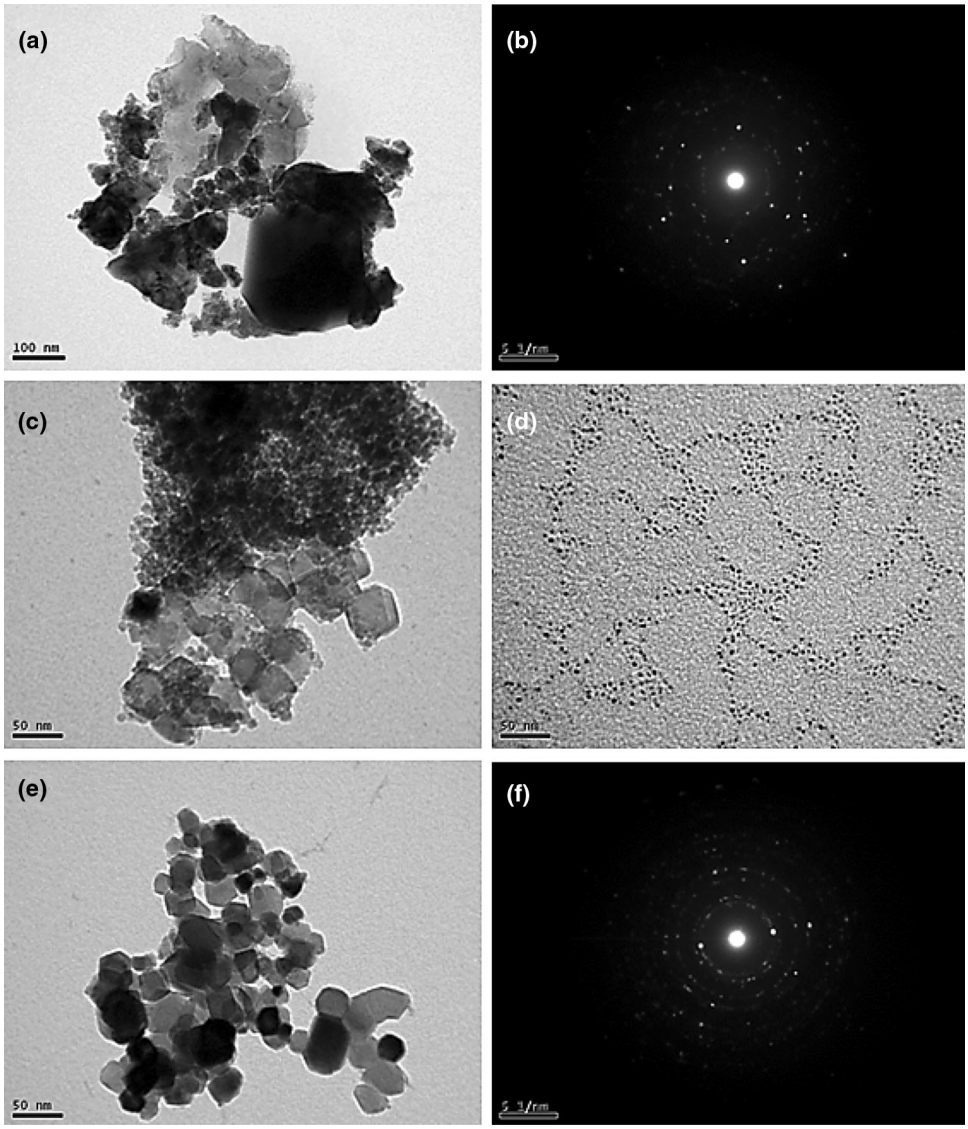

Fig. 7 TEM images and electron diffraction patterns of the SnO_2 obtained from $SnCl_2$·Chitosan having [polymer/metal] molar ratio of 1:1 (**a**, **b**);1:5 (**c**, **d**); and 1:10 (**e**, **f**)

(1:1 $ZnCl_2$·Chitosan precursor), 2.16 (1:5 $ZnCl_2$·Chitosan precursor) and 2.26 eV (1:10 $ZnCl_2$·Chitosan precursor). The values are slightly different depending on the [polymer/metal] molar ratio of the $ZnCl_2$·Chitosan precursors. Furthermore, the values are lower than that reported for bulk samples of ZnO (3.37 eV), and also lower with respect to ZnO materials prepared by related methods [36, 37], which can be explained by the high crystallinity and large particle size aggregates observed in the electron diffraction patters and TEM micrograph respectively (see Fig. 2) [38, 39]. Additionally, the presence of residual carbon impurities [36] and the high temperatures used during the ZnO formation [37], can be also accounted for the low values of the E_g obtained.

The photoluminescence spectra of the as prepared ZnO materials (Fig. 5), showed four different emission peaks at 354, 392–395, 423, and 566–573 nm. By comparison with the emission spectra pattern of ZnO materials obtained by related methods, these emission peaks are assigned as follows: The strong Uv–vis bands at 354 and 392 nm correspond to the exciton recombination related to the near-band edge (NBE) emissions of ZnO; the blue emission (423 nm) corresponds to the electron transition to the conductive band to interstitials oxygen defects (O_{in}) in the ZnO; and finally, the observed emission band at 560 nm (green emission) could be assigned to a several effects such as the transition between singly charged oxygen vacancy and photo excited hole [40, 41], the transition between the electron close to the conduction band and deeply trapped hole at V_o^{++} center (oxygen vacancy containing no electrons) [42–44], the donor–acceptor and shallow donor–deep level transitions [45–47], the zinc interstitials [48], and the oxygen antisites [49]. Similar photoluminescence peaks have been obtained for ZnO B-doped materials [50].

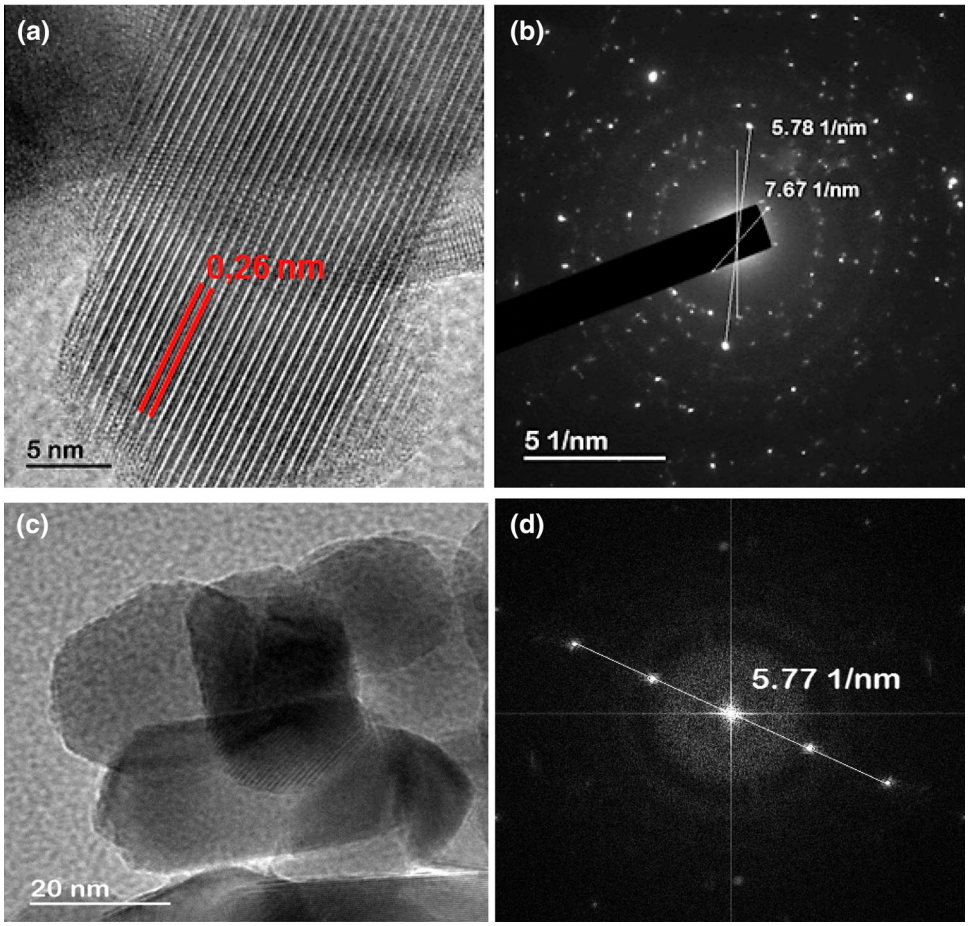

Fig. 8 HR-TEM (**a**, **c**) and electron diffraction patterns (**b**, **d**) images of SnO_2 prepared from the 1:1 precursor $SnCl_2$·Chitosan

The XRD pattern analysis for the pyrolytic products from precursor $SnCl_2$·Chitosan in [polymer/metal] molar ratios of 1:1, 1:5, and 1:10, showed the presence of pure SnO_2 cassiterite-synphase. The main observed reflections at $2\theta = 26.08°$, 33.89°, 37.96°, 51.80° and 54.67° can be indexed to the spacing (110), (101), (200), (211) and (220) respectively (see Figure S6 in the Supplementary Data).

The analysis of the as prepared SnO_2 cassiterite-synphases by SEM, clearly showed dependence of the morphology with the [polymer/metal] molar ratio of the precursors $SnCl_2$·Chitosan (Fig. 6). Thus, when $SnCl_2$·Chitosan having [polymer/metal] molar ratio of 1:1 was used as precursor, the SEM images showed a non-compacted porous materials having a foam-like texture (see Fig. 6a), whereas when the 1:5 and 1:10 [polymer/metal] molar ratios of the $SnCl_2$·Chitosan precursor was used, mixtures of foam-like textures and rod-like nanostructures were clearly observed (see Fig. 6b–c in which nanorod are highlighted with white arrows).

SnO_2 materials were analyzed by TEM observing a slightly different size distribution of the nanostructures depending of the different [polymer/metal] molar ratios used in the $SnCl_2$·Chitosan precursors (see Fig. 7). Thus, the smallest size SnO_2 nanoaggregates were observed when a 1:5 [polymer/metal] molar ratio of the $SnCl_2$·Chitosan precursor was used (see Fig. 7c). Interestingly, at this [polymer/metal] molar ratio of the $SnCl_2$·Chitosan precursor (1:5), we observed areas in which very small and almost uniform SnO_2 nanoparticles were formed (particle diameter average of 2.1 ± 0.2 nm). Moreover, these small size nanoparticles exhibited a directional dispersity probably due to the dewetting of the solvent during the casting of the sample over the carbon coated copper grid (see Fig. 7d). The electron diffraction pattern of the SnO_2 material obtained from the different $SnCl_2$·Chitosan precursors evidenced the crystalline nature of the pyrolytic SnO_2 products obtained by this methodology (see Fig. 7f).

HRTEM analysis was performed using a single crystal SnO_2 nanoparticle obtained from the 1:1 $SnCl_2$·Chitosan precursor (see Fig. 8a). The measured lattice spacing of adjacent lattice planes was about 0.26 nm, which corresponds to the (101) plane of tetragonal SnO_2 nanoparticles cassiterite-synphase, and grew along the [101] direction. The polycrystalline-line diffraction rings of electron diffraction pattern patterns (see Fig. 8b, d) also demonstrate the microstructural character of the typical

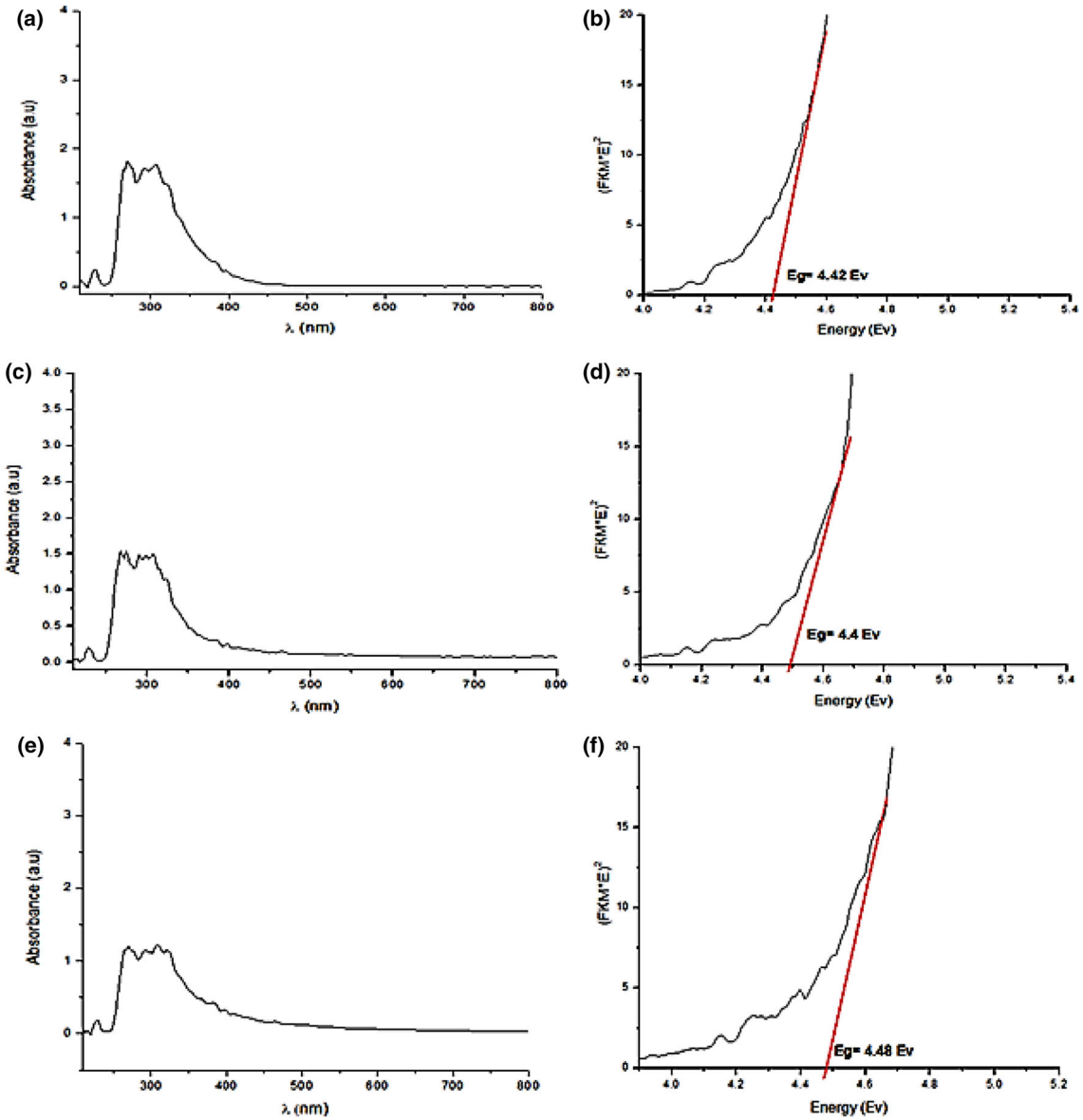

Fig. 9 UV-vis absorption and reflectance data (converted to Kubelka–Munk spectra) of SnO_2 nanoparticles created by the $SnCl_2$·Chitosan precursors at different [polymer/metal] molar ratios: **a** 1:1, **c** 1:5, and **e** 1:10. Tauc's plot, $(\alpha h\nu)^2 = A(h\nu - E_g)$ having the optical band energy (E_g) of SnO_2 nanoparticles created by the $SnCl_2$·Chitosan precursors at different [polymer/metal] molar ratios: **b** 1:1, **d** 1:5, and **f** 1:10

tetragonal cassiterite SnO_2 phase ($d_{101} = 0.26$ nm and $d_{110} = 0.34$ nm).

We studied the diffuse reflectance spectra (DRS) of the SnO_2 materials prepared from the 1:1. 1:5 and 1:10 $SnCl_2$·Chitosan precursors at room temperature (see Fig. 9a, c and e. The reflectance data was converted to Kubelka–Munk equation using standard procedures). SnO_2 materials showed a strong and broad absorption banding the region from 200 to 400 nm, being located the maximum of the absorption band at ca. 250 nm. The optical band gap energies of the products were estimated from Tauc's plot, (see Fig. 9b, d and f). The band gap values of the E_g were found to be 4.42 (1:1 $SnCl_2$·Chitosan precursor), 4.40 (1:5 $SnCl_2$·Chitosan precursor), and 4.48 eV (1:10 $SnCl_2$·Chitosan precursor). The values are slightly different depending on the [polymer/metal] molar ratio of the $SnCl_2$·Chitosan precursors. The values are higher than those reported for bulk samples of SnO_2 (3.64 eV), and also higher than those of the SnO_2 materials prepared by related methods [51, 52]. These higher values of the E_g of the as synthesized SnO_2 materials can be related with the large particle size aggregates observed in the TEM micrographs (see Fig. 7), and the high temperature used during the pyrolysis process [51].

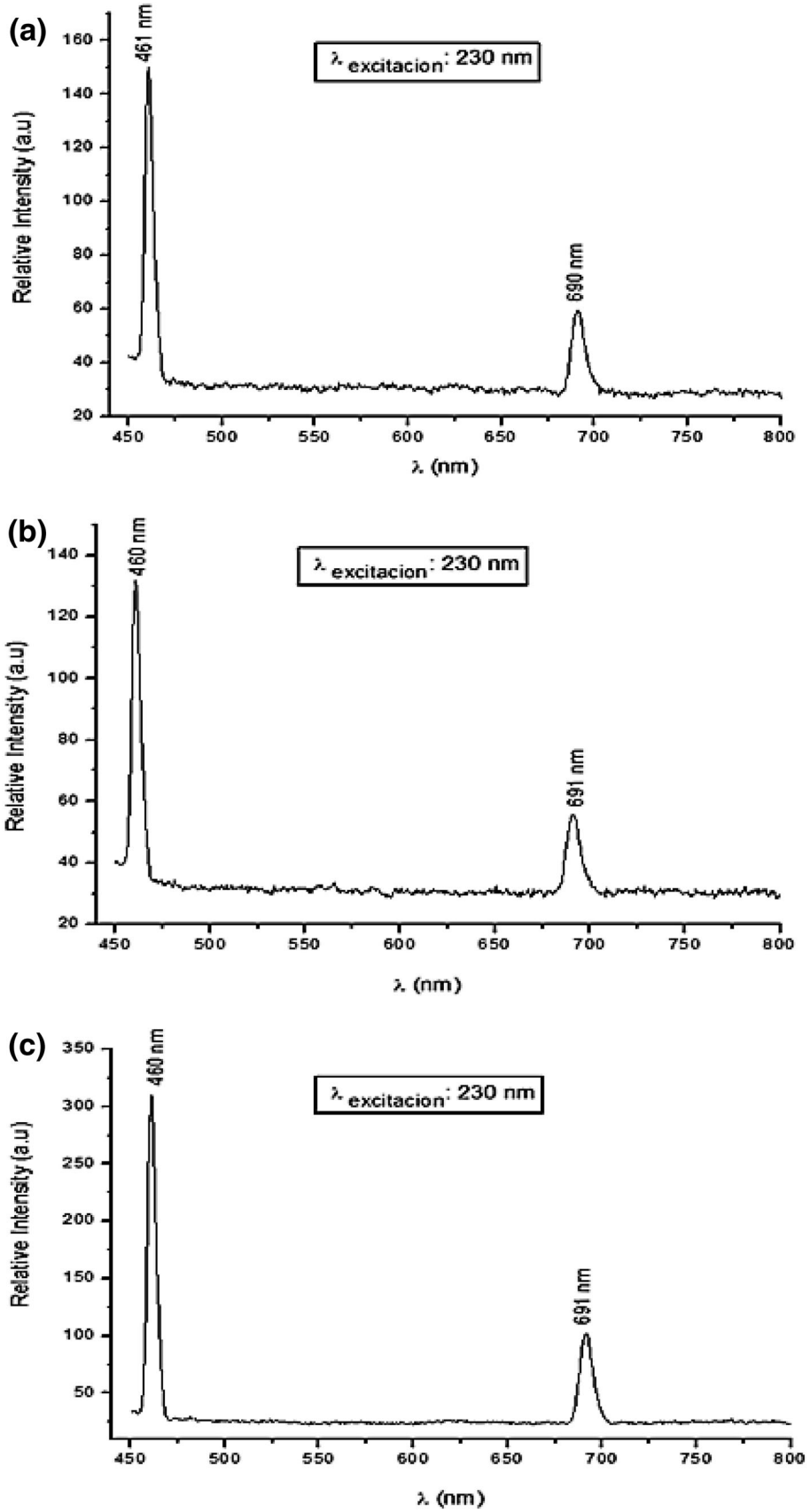

Fig. 10 Luminescence spectra of SnO_2 nanoparticles created by pyrolysis of the $SnCl_2$·Chitosan precursors having different [polymer/metal] molar ratios: **a** 1:1, **b** 1:5, and **c** 1:10

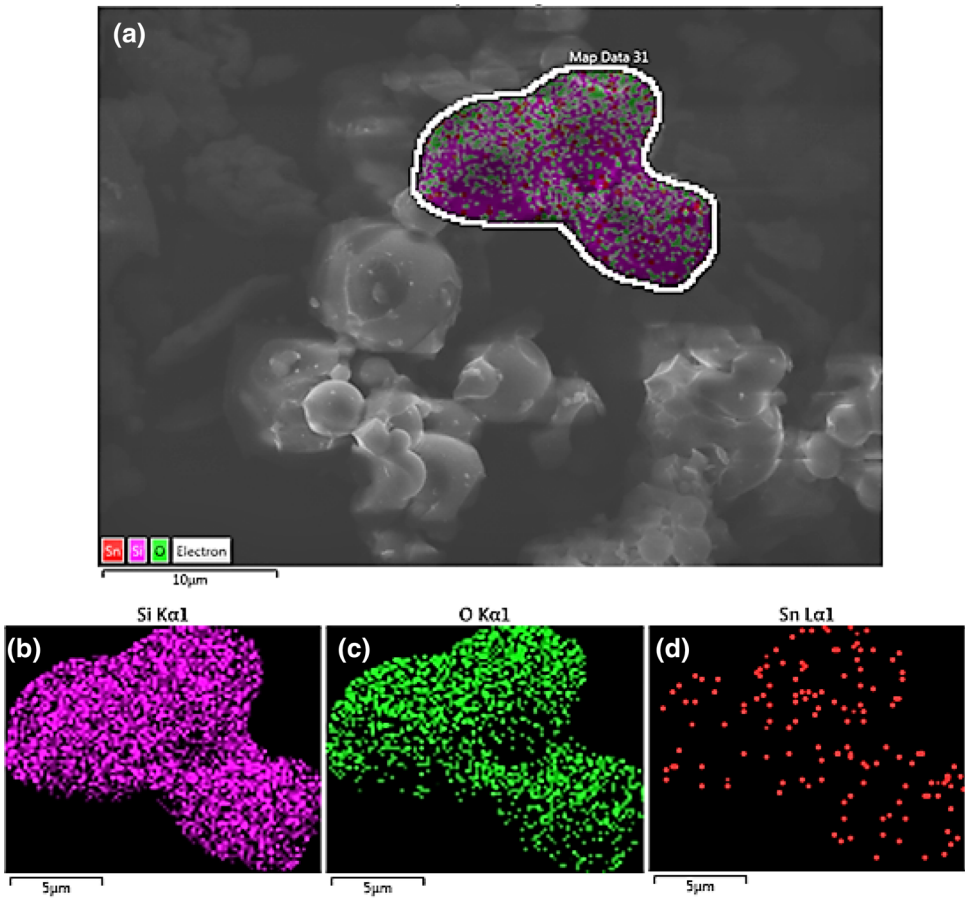

Fig. 11 SEM analysis of SnO_2//SiO_2 materials showing an EDS mapping analyses of elements in a grain of material. Elements: Sn (red), Si (purple), and oxygen (green) (Color figure online)

The photoluminescence spectra of the as prepared SnO_2 exhibited an intense blue luminescence at a wavelength of 460 nm (see Fig. 10), which may be attributed to oxygen-related defects that have been introduced during the growth process [52–54]. Furthermore, an additional weak emission at 690 nm was observed (see Fig. 10), which can be attributed to small traces of impurities during sample preparation [53].

Incorporation of ZnO and SnO_2 into SiO_2 was achieved by pyrolysis of mixtures of MCl_2·Chitosan (M=Zn and Sn) precursors and SiO_2 (SiO_2 was synthesized by a sol–gel method). The XRD diffraction patterns of the isolated products (see Figure S7 in Supplementary Data) obtained after the pyrolysis, showed the peaks corresponding to the incorporation of SnO_2 into the SiO_2 (SnO_2//SiO_2). However, the pyrolysis of the mixtures $ZnCl_2$·Chitosan and SiO_2 led to Zn_2SiO_4 and SiO_2 (see XRD in Figure S7). The SnO_2//SiO_2 material was further analyzed by SEM and EDS mapping (Fig. 11). The images clearly showed the presence of SnO_2 homogeneously distributed into the SiO_2 matrix (see Fig. 11). The UV–visible diffuse reflectance spectra of the SnO_2//SiO_2 materials were very similar to that of pure SnO_2 (i.e. without SiO_2) [52–54], and similar to that different SnO_2//SiO_2 materials prepared by related synthetic methodologies [55]. The band gap value estimated using the Tauc approximation for SnO_2//SiO_2 materials was 3.1 eV, significantly lower than that obtained for pure SnO_2 prepared by pyrolysis (ca. 4.4 eV, see discussion above). This lower value might be due to the presence of the amorphous silica that precludes the formation of large SnO_2 nanoparticles (see the Sn mapping in Fig. 11), leading, therefore, to E_g value very similar to that of the pure SnO_2 (ca. 3.0 eV) [51].

The photoluminescence spectrum of SnO_2//SiO_2 (see Figure S8 in the Supplementary Data) exhibited a strong near-Uv luminescence emission (ca. 400 nm), which is very similar to that observed in SnO_2//SiO_2 obtained by solution methods [55]. However, some important differences can be observed with respect to the luminescence spectrum of pure SnO_2 obtained by direct pyrolysis of the $SnCl_2$·Chitosan precursors. The emission peak observed at 690 nm for the last was not observed in the spectrum of the SnO_2 included in SiO_2. Also the emission peak at 420 nm observed for pure SnO_2 was shifted to 400 nm. These changes are due to the different oxygen-related defects that have been introduced during the inclusion process.

Although the formation of single phase crystalline nanoparticles in solution is well-known [56, 57] under a

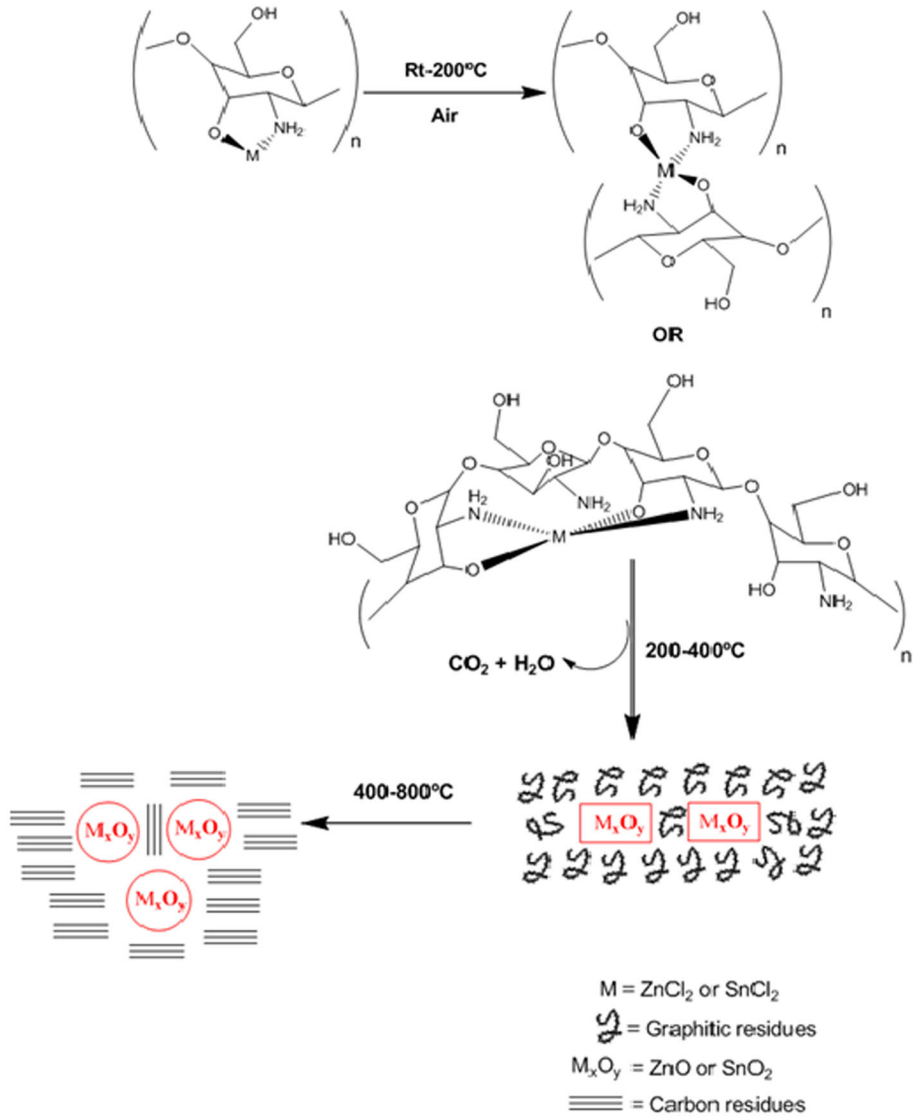

Fig. 12 Schematic Representation of the possible mechanism of formation of ZnO and SnO_2 nanoparticles

variety of conditions, the formation mechanism in solid-state is lacking [58, 59] and its development is important for materials that are sensitive to liquid/solvent environments, or that require a demixing-mediated crystallization process that infers thorough porosity throughout the powder. The formation mechanism of the solid-state ZnO and SnO_2 nanostructures in this work can be compared to comparative investigations [16]. The first step on heating involves the formation of a 3D network to produce a thermal [15] stable matrix, shown in Fig. 12. This step is crucial to offset sublimation. For instance, ferrocene undergoes sublimation on heating at 483 K (the melting point), but in presence of oxalic acid nanoparticles of Fe_2O_3 nanoparticles are formed [59]. In our system, the first heating step likely involves a cross-linking of the Chitosan precursors to give a 3D matrix containing O–M–O, H_2N–M–NH_2 as well as O–M–NH_2 links M=Zn and Sn. A schematic representation of this process is shown in Fig. 12. The following steps involve the initiation of the organic carbonization, holes or voids are produced where the nanoparticles of ZnO and SnO_2 are able to nucleate. According to TG/DSC analysis this occurs at $\sim$ 400 °C for the Chitosan matrices (see Figure S4 in Supplementary Materials). Simultaneously, the oxygen of the air form ZnO and SnO_2 that nucleates inside the holes formed by the combustion of the organic matter. In this intermediate stage a layered graphitic carbon host was detected [16] that acts as template were the nanoparticles can coalesce and crystallize into their respective morphologies. After complete combustion, this template is fully decomposed, forming a residual carbon that appears as an ultrathin carbon shell surrounding the nanoparticles [13].

Conclusions

Nanoparticles of ZnO and SnO_2 have been conveniently prepared by the pyrolysis (800 °C, air) of hybrid macromolecular precursors $ZnCl_2$·Chitosan and $SnCl_2$·Chitosan having different [polymer/MCl_2] (M=Zn or Sn) ratios (1:1, 1:5 and 1:10). The morphology and size of the nanostructured ZnO and SnO_2 materials can be controlled by varying the [polymer/MCl_2] ratio in the MCl_2·Chitosan (M=Zn, Sn) precursors. Thus, the smallest size oxides were obtained by using the 1:5 polymer/metal ratios. As prepared ZnO materials exhibit luminescence spectra having the most intense emission at 440 nm, which corresponds to a radiative transition of an electron from the shallow donor level of oxygen vacancies, and the zinc interstitial, to the valence band. Furthermore, ZnO materials show a rather intense green emission at ca. 573 nm, which is characteristic of this synthetic methodology. On the other hand, the photoluminescence spectrum of the nanostructured SnO_2 shows an intense blue luminescence at a wavelength of 420 nm which may be attributed to oxygen-related defects that have been introduced during the growth process of the nanoparticles. The absorption and luminescence properties of as prepared ZnO and SnO_2 materials showed a very small dependence of the [polymer/metal] molar ratio of the MCl_2·Chitosan (M=Zn, Sn) precursors used in their preparation. In other hand, whereas SnO_2 was successfully incorporated into SiO_2 structure (SnO_2//SiO_2) by pyrolysis of solid-state mixtures of the precursors $SnCl_2$·Chitosan in the presence of SiO_2, the same reaction carried out with $ZnCl_2$·Chitosan precursors led to a mixture of Zn_2SiO_4 and SiO_2. The absorption and photoluminescence properties of the nanostructured SnO_2//SiO_2 were very similar than those of pure SnO_2. Although the morphology and size control by this method is only partial, this is good progress with regard the second step is high thermal process where almost null size and morphology control has been achieved.

Supplementary Data

Experimental details, ^{13}C CP-MAS NMR spectroscopy, XRD patterns, EDX analysis, and TGA/DTA curves of the MCl_2·Chitosan (M=Zn and Sn) precursors, and metal oxide (ZnO and SnO_2) materials, are included. Also XRD of SnO_2//SiO_2 and $ZnSiO_4$: SiO_2: ZnO//SiO_2 composites and the Photolumincense spectrum of SnO_2//SiO_2 are included.

Acknowledgements C.D. is grateful to Fondecyt (Project 1160241) for the funding. A.P.S. is grateful to FICYT (Projects SV-PA-13-ECOEMP-83 and FC-15-GRUPIN14-106), Universidad de Oviedo (Project UNOV-13-EMERG-GIJON-08) and the MINECO (Project CTQ2014-56345-P) for the funding. A.P.S.is also grateful to the COST action Smart Inorganic Polymers (SIPs-CM1302—http://www.sips-cost.org/home/index.html), and the Juan de la Cierva and Ramón y Cajal programs.

References

1. R. K. Joshi and J. J. Schneider (2012). *Chem. Soc. Rev.* **41**, 5285–5312.
2. P. Poizot, L. S. Grugeon, L. Dupont, and J. M. Tarascon (2000). *Nature* **407**, 496–499.
3. Y. Li and G. A. Somorjai (2010). *NanoLetter* **10**, 2289–2295.
4. Q. Zhang, H. Y. Wang, J. Xinli, and Y. Yang (2013). *Nanoscale* **5**, 7175–7183.
5. H. Wang and A. L. Rogach (2014). *Chem. Mater.* **26**, 123–133.
6. M. Ahmad and J. J. Zhu (2011). *J. Mater. Chem.* **21**, 599–615.
7. A. Tricoli, M. Righettoni, and A. Teleki (2010). *Angew. Chem. Int. Ed.* **49**, 7632–7659.
8. V. Juttukonda, R. L. Paddock, J. E. Raymond, D. Denomme, A. E. Richardson, L. Slusher, and B. D. Fahlman (2006). *J. Am. Chem. Soc.* **128**, 420–421.
9. J. Q. Sun, J. S. Wang, X. C. Wu, G. S. Zhang, J. Y. Wei, S. Q. Zhang, H. Li, and D. R. Chen (2006). *Cryst. Growth Des.* **6**, 1584–1587.
10. M. Salvat-Niasari, N. Mir, and F. Davar (2010). *Inorg. Chim. Acta* **363**, 1719–1726.
11. M. Zereie, A. Gholami, M. Bahrami, and A. H. Rezaei (2013). *Mater. Lett.* **91**, 255–257.
12. M. Hossienifard, L. Hashemi, V. Amani, K. Kalatech, and A. Morsali (2011). *J. Inorg. Organomet. Polym.* **21**, 527–533.
13. C. Díaz and M. L. Valenzuela in H. S. Nalwa (ed.), *Encyclopedia of Nanoscience and Nanotechnology*, vol. 16 (American Scientific, Valencia, 2011), pp. 239–256.
14. C. Díaz and M. L. Valenzuela (2006). *J. Inorg. Organomet. Polym.* **16**, 419–435.
15. C. Díaz, M. L. Valenzuela, L. Zuñiga, and C. O'Dwyer (2009). *J. Inorg. Organomet. Polym. Mater.* **19**, 507–520.
16. C. Díaz, M. L. Valenzuela, V. Lavayen, and C. O'Dwyer (2012). *Inorg. Chem.* **51**, 6228–6236.
17. C. Díaz, G. A. Carriedo, M. L. Valenzuela, L. Zuñiga, and C. O'Dwyer (2012). *J. Inorg. Organomet. Polym. Mater.* **22**, 447–454.
18. C. Díaz, M. L. Valenzuela, S. Cáceres, and C. O´Dwyer (2013). *J. Mater. Chem. A* **11**, 1566–1572.
19. W. S. Wan-Ngah, L. C. Teong, and M. A. Hanafiah (2011). *Carbohydr. Polym.* **83**, 1446–1452.
20. I. Aranaz, M. Mengibar, R. Harris, I. Paños, B. Miralles, N. Acosta, G. Galed, and A. Heras (2009). *Curr. Chem. Biol.* **3**, 203–230.
21. K. Okuyama, K. Noguchi, T. Miyazawa, T. Yui, and K. Ogawa (1997). *Macromolecules* **30**, 5849–5855.
22. K. Mazeau, W. T. Winter, and J. H. Chanzy (1994). *Macromolecules* **27**, 7606–7612.
23. A. Muzzarelli *Chitin* (Pergamon Press, New York, 1973).
24. R. M. Majeti and R. Kumar (2000). *React. Funct. Polym.* **46**, 1–27.
25. M. Kong, X. G. Chen, K. Xing, and H. J. Park (2010). *Int. J. Food Microbiol.* **144**, 51–63.
26. G. Crini and P. M. Badot (2008). *Prog. Polym. Sci.* **33**, 399–447.
27. F. Chin, R. L. Tseng, and R. S. Juang (2010). *J. Environ. Manag.* **91**, 798–806.
28. A. A. Emara, M. A. Tawad, M. A. El-ghamry, and M. Z. Elsabee (2011). *Carbohydr. Polym.* **83**, 192–202.
29. K. Ozawa, K. Oka, and T. Yui (1993). *Chem. Mater.* **5**, 726–728.

30. S. Schlick (1986). *Macromolecules* **19**, 192–195.
31. M. Rinaudo (2006). *Prog. Polym. Sci.* **31**, 603–632.
32. A. Sine, B. O. Petersen, J. O. Duus, and T. Skrydstrup (2007). *Inorg. Chem.* **46**, 4326–4334.
33. L. Heux, J. Brugnerotto, J. Desbrieres, M. F. Versali, and M. Rinaudo (2000). *Biomacromolecules* **1**, 746–751.
34. D. De Brito and S. P. Campana-Filho (2007). *Thermochim. Acta* **465**, 73–79.
35. M. Anandam, S. Dinesh, and N. J. Krishnakumar (2017). *Mater. Sci. Mater. Electron.* **28**, 2574–2585.
36. M. Samadi, H. Asghari, A. Pourjavadi, and A. Z. Moshfegh (2013). *Appl. Catal. A* **466**, 153–160.
37. R. Vinodkumar, I. Navas, K. Porsezian, V. Ganesan, N. V. Unnikrishnan, and V. P. Pillai (2014). *Spectrochim. Acta A* **118**, 724–732.
38. K. Sowri-Babu, A. Ramachandra Reddy, C. Sujatha, V. Venugopal Reddy, and A. N. Mallika (2013). *J. Adv. Ceram.* **2**, 260–265.
39. J. P. Mathewa and G. Vargheseb (2012). *Chin. Phys. B* **21**, 781041–781048.
40. K. Vanheusden, C. H. Seager, W. L. Warren, D. R. Tallant, and J. A. Voigt (1996). *Appl. Phys. Lett.* **68**, 403–405.
41. K. Vanheusden, W. L. Warren, C. H. Seager, D. R. Tallant, J. A. Voigt, and B. E. Gnade (1996). *J. Appl. Phys.* **79**, 7983–7990.
42. A. Van Dijken, E. Meulenkamp, D. Vanmaekelbergh, and A. Meijerink (2000). *J. Phys. Chem. B* **104**, 1715–1723.
43. A. Van Dijken, E. Meulenkamp, D. Vanmaekelbergh, and A. Meijerink (2000). *J. Lumin.* **90**, 123–128.
44. A. Wood, M. Giersig, M. Hilgendorff, A. Vilas-Campos, L. M. Liz-Marzán, and P. Mulvaney (2003). *Aust. J. Chem.* **56**, 1051–1057.
45. D. C. Reynolds, D. C. Look, B. Jogai, and H. Morkoç (1997). *Solid State Commun.* **101**, 643–646.
46. S. A. Studenikin and M. Cocivera (2002). *J. Appl. Phys.* **91**, 5060–5065.
47. D. C. Reynolds, D. C. Look, and B. Jogai (2001). *J. Appl. Phys.* **89**, 6189–6191.
48. M. Liu, A. H. Kitai, and P. Mascher (1992). *J. Lumin.* **54**, 35–42.
49. B. Lin, Z. Fu, and Y. Jia (2001). *Appl. Phys. Lett.* **79**, 943–975.
50. P. Gomathisankar, K. Hachisuka, H. Katsumata, T. Suzuki, K. Funasaka, and S. Kaneco (2013). *ACS Sustain. Chem. Eng.* **1**, 982–988.
51. P. Chetri and A. Choudhury (2013). *Physica E* **47**, 257–263.
52. V. Rajendran and K. Anandan (2012). *Mater. Sci. Semicond. Process.* **15**, 393–400.
53. Y Ch HeR and J. Y. Hu (2006). *Appl. Phys. Lett.* **89**, 043115-1–043115-3.
54. B. Liu, C. W. Cheng, R. Chen, Z. X. Shen, H. J. Fan, and H. D. Sun (2010). *J. Phys. Chem.* **114**, 3407–3410.
55. Z. C. Liu, H. R. Chen, W. M. Huang, J. L. Gu, W. B. Bu, Z. L. Hua, and J. L. Shi (2006). *Micropor. Mesopor. Mater.* **89**, 270–275.
56. F. Wang, V. N. Richard, S. P. Shieds, and W. E. Buhro (2014). *Chem. Mater.* **26**, 5–21.
57. E. Finney and R. Finke (2008). *J. Colloid Interface Sci.* **317**, 351–374.
58. C. Díaz and M. L. Valenzuela in H. S. Nalwa (ed.), *Metallic Nanostructures Using Oligo and Polyphosphazenes as Template or Stabilizer in Solid State in Encyclopedia of Nanoscience and Nanotechnology* (American Scientific Publishers, Valencia, 2010).
59. A. Bhattacharjee, A. Rooj, M. Roy, J. Kusz, and P. Guthich (2013). *J. Mater. Sci.* **48**, 2961–2968.